

Surface-Current Measurements as Data for Electromagnetic Imaging Within Metallic Enclosures

Mohammad Asefi, *Student Member, IEEE*, Gabriel Faucher, and Joe LoVetri, *Senior Member, IEEE*

Abstract—A 3-D microwave imaging method within metallic enclosures is investigated and improved. This method uses the components of the surface-current vector at receiver points on the enclosure wall as data. At the metallic wall, the normal component of the magnetic field as well as the tangential components of the electric field is negligible, whereas the vectorial surface current, which is directly related to the tangential components of the magnetic field, is dominant. After presenting the results of a numerical investigation based on synthetic data, the method is validated using an experimental system comprised of 24 co-resident shielded, coaxial half-loop antennas, distributed in four layers, within a cylindrical metallic enclosure. These antennas are used in receiver-transmitter pairs to introduce an electromagnetic field into the chamber and collect the magnetic field at the receiver points. The measured data are used as input to a multiplicatively regularized finite-element contrast source inversion algorithm. Due to their relatively small size and minimal protrusion into the chamber, these antennas minimally perturb the field distribution inside the chamber and thereby allow the use of a simple numerical inversion model, which does not need to account for the passive antennas. These attributes are especially useful for large computationally intensive industrial applications. The experimental system described herein is a laboratory-scale prototype for a stored-grain imaging application where metallic silos are utilized.

Index Terms—Inverse scattering problems, magnetic field, microwave imaging (MWI), modeling error reduction, PEC imaging, surface-current imaging, surface-current measurement, 3-D imaging.

I. INTRODUCTION

MICROWAVE imaging (MWI) is a modality that utilizes electromagnetic radiation to obtain information about the electrical properties of the internal structure of a region-of-interest (RI). Depending on the application and type of the imaging system, this information can either be *qualitative* or *quantitative*. In most cases, the former provides an insight to the interior and/or surface of the RI via either a map of the distribution of the intensity of the electric field or the qualitative scattering properties within the RI. Two applications of the qualitative methods are nondestructive testing and evaluation

of material [1], [2] and concealed weapon detection [3]. Quantitative imaging, on the other hand, provides a numerical map of the complex dielectric properties of the RI and can therefore better characterize the inhomogeneities within the RI. This makes such systems of interest for a wide range of industrial and biomedical applications [4]–[8].

Many industrial sectors, such as the oil and gas industry, and the agricultural and food sectors, store and/or transfer their products in large metallic containers/pipelines. Unexpected anomalies within the bulk product when stored or transferred can have significant impact on the quality of the products. For example, in agriculture, after grain is harvested, it is stored in large metallic containers, and different external agents as well as temperature/moisture variations can cause mold formation [9]. Thus, monitoring the products for (early) detection of abnormalities within the bulk product is valuable to such industries.

Some of the important requirements for any monitoring system, including any potential MWI monitoring system applicable to these industries, are the capability of functioning within the electrically shielded structures, mechanical characteristics that ensure its functionality in harsh environments, and that there be minimal modifications to the existing apparatus. Typically, any MWI system introduces an electromagnetic measurement system that includes antennas and a transceiver unit to collect data [1], [6], [10]. Therefore, meeting these requirements can be quite challenging.

Due to the use of side mounted antennas, MWI can be a viable solution to provide a 3-D map of the interior of electrically shielded structures, such as within storage containers and pipelines. The Electromagnetic Imaging Laboratory (EIL) at the University of Manitoba has had success in developing the MWI systems for different applications and has recently demonstrated the use of the normal component of the electric field inside the metallic chambers as data for MWI [11], [12]. The system described in [11] uses reconfigurable monopole antennas (RAs) distributed on the internal surface of the chamber walls of a cylindrical enclosure to excite and collect electric fields within the chamber. Because of the high quality factor of the metallic enclosures, the field inside such chambers is sensitive to small changes, which makes modeling such systems challenging. It was shown that the use of RAs helps in reducing the modeling error while maintaining the sensitivity of the antennas. MWI using the normal component of the electric is viable, because it is the only component of the

Manuscript received November 17, 2015; revised March 1, 2016, April 12, 2016, August 8, 2016, and August 15, 2016; accepted August 17, 2016. Date of publication September 16, 2016; date of current version November 3, 2016.

The authors are with the Department of Electrical and Computer Engineering, University of Manitoba, Winnipeg, MB R3T 5V6, Canada (e-mail: joe_lovetri@umanitoba.ca).

Color versions of one or more of the figures in this paper are available online at <http://ieeexplore.ieee.org>.

Digital Object Identifier 10.1109/TMTT.2016.2605665

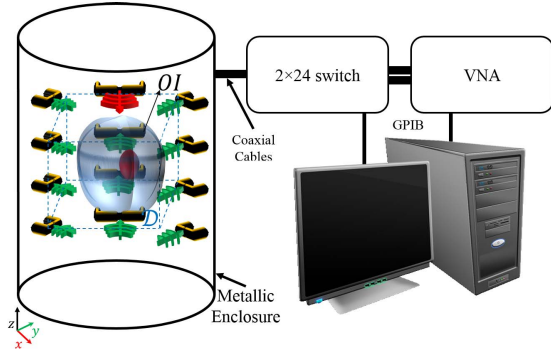


Fig. 1. Block diagram of the 3-D MWI system including the imaging chamber and the antennas.

electric field that exists at a metallic surface (to a good approximation). However, this provides only one piece of data, whereas the two existing polarizations of the magnetic field can provide two pieces of independent data. In fact, each tangential component of the magnetic field, which directly corresponds to a component of the surface current, is related to the normal component of the electric field via a spatial derivative on the surface. Therefore, a minimum of two normal components of the electric field would need to be measured in order to obtain a coarse approximation of one of the tangential magnetic field components. If the magnetic field components at the walls could be measured directly, this opens the possibility of obtaining a better set of inversion data. The coaxial shielded half-loop antennas introduced herein provide a viable approach for such measurements.

In addition to the electromagnetic perspective, the significant physical protrusion into the environment being imaged of any of the utilized antennas limits their use for many industrial applications where the content of the containers or pipelines would exert excessive forces on the antennas. These forces exist, for example, because of the movement or excessive weight of the commodity being stored or transferred. The proposed low-profile coaxial half-loop antennas exhibit good mechanical features, which mitigate against these forces.

The focus of this paper is on grain imaging within metallic enclosures. The block diagram of a typical system configuration is shown in Fig. 1 where a series of antennas mounted to the walls of the chamber collect electromagnetic field data, which is then inverted using an inversion algorithm. Although the details of the inversion algorithm are not within the scope of this paper, in Section II, the basic features of the utilized algorithm are described. The main contribution of the paper is the feasibility of using tangential surface currents as data for this inversion algorithm. In Section III, results of a synthetic analysis of the proposed method are presented. The practical viability of such a system is investigated using a laboratory-scale prototype described in Section IV. In this section, we also describe the coaxial shielded half-loop antennas that were utilized as well as the calibration technique used on the collected data.

II. NUMERICAL MODELING AND INVERSION

In order to study the performance of the proposed imaging system synthetically and experimentally, a numerical MWI

algorithm is required. The finite-element contrast source inversion (FEM-CSI) algorithm developed in the EIL allows for utilizing both electric and magnetic dipoles as sources and can calculate the electric field everywhere within the imaging domain inside the discretized model of the system [11], [13]. Thus, it can be utilized for both numerical generation of the scattered field data for an object-of-interest and inversion of the synthetically generated or measured data.

In the aforementioned FEM-CSI algorithm, both types of sources are modeled as infinitesimal Hertzian dipoles (magnetic or electric current sources). If the current density for such an electric source, \vec{J}_t , denotes the unit vector along the desired polarization and located at position \vec{V}_t , the electric field produced by this source can be calculated as

$$\vec{E}_t(\vec{V}) = -j\omega\mu_0\vec{J}_t \cdot \vec{G}(\vec{V}, \vec{V}_t) \quad (1)$$

where $\vec{G}(\vec{V}, \vec{V}_t)$ is the dyadic Green's function for an unbounded homogeneous medium and the $e^{j\omega t}$ time dependence is assumed. This Green's function is calculated as

$$\vec{G}(\vec{V}, \vec{V}_t) = \left(\vec{I} + \frac{\nabla\nabla}{k^2} \right) \frac{e^{-jk|\vec{V}-\vec{V}_t|}}{4\pi|\vec{V}-\vec{V}_t|}. \quad (2)$$

The field inside the chamber, for this source, is first calculated using the scattered-field formulation where the chamber walls and/or material partially filling the chamber are considered to be the scatterers. For the case where magnetic dipole sources are required, they are modeled by applying duality to the electromagnetic expressions given in (1).

The FEM code solves the second-order vector Helmholtz equation for the electric field using the first-order edge elements on tetrahedra [13], [14]. The electric field at a point, $\vec{r} = [x, y, z]$, within the FEM computational domain is calculated via the basis functions

$$\vec{E}(\vec{r}) = \sum_{i=1}^6 u_i^e \vec{N}_i^e(\vec{r}) \quad (3)$$

where u_i^e and \vec{N}_i^e are, respectively, the tangential field and first-order vector basis function along edge i of element e . Element e is chosen, such that it contains the point denoted by \vec{r} . Thus, if any electric field component is required during the forward solve or the inversion process, such as E_ρ , this can be directly constructed using the basis functions. However, when magnetic field components are required, these need to be constructed using the electric field solution. The approach taken here is to apply Faraday's Law to the electric field solution

$$\vec{H}(\vec{r}) = -\frac{\nabla \times \vec{E}(\vec{r})}{j\omega\mu} \quad (4)$$

which can then be directly applied to the basis-vector expansion of $\vec{E}(\vec{r})$. The resulting equation becomes

$$\vec{H}^e = \frac{-1}{j\omega\mu} \sum_{i=1}^6 u_i^e \nabla \times \vec{N}_i^e(\vec{r}). \quad (5)$$

Additional details on contrast source inversion algorithms can be found in [14] and [15].

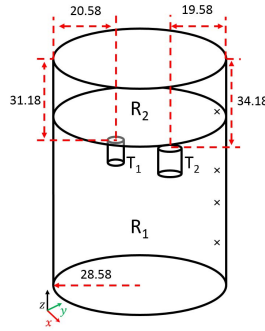


Fig. 2. Imaging chamber including the targets T_1 and T_2 . X marks the location of the transmitters and receivers along the height of the chamber. All dimensions are in cm.

III. SYNTHETIC ANALYSIS

To confirm the feasibility of using the surface currents as data for microwave inversion, synthetic results that compare the imaging performance between using various polarizations of the surface currents and using the normal component of the electric field at the same receiver locations are presented. Using synthetic experiments emphasizes the comparison on the numerical aspects of the problem rather than the experimental implementation and performance of the actual antennas.

Multiple synthetic examples incorporating two simple numerical targets within an open-top as well as a closed-top cylindrical metallic enclosure were investigated. The PEC enclosure for this synthetic study has a radius of 28.58 cm and a height of 86.36 cm. Note that if the empty chamber is thought of as an open-ended waveguide, the first resonant mode will be the TE_{11} mode with a resonant frequency of 301 MHz and if it is thought of as a closed resonant cavity, the first resonant mode will be TE_{111} having a resonant frequency of 347.2 MHz. Two regions are defined within the chamber, R_1 and R_2 , allowing the modeling of either an empty or partially filled chamber (these are shown in Fig. 2). For the partially filled case, the complex dielectric constant of region R_1 is set to $\epsilon_{\text{real}} - j\epsilon_{\text{imaginary}} = 2.96 - j0.288$ (a typical value for hard red winter wheat with 9% moisture content) while region R_2 is set to air.

All synthetic examples contain two targets. Their location within the metallic chamber is shown in Fig. 2. Target T_1 has a diameter of 6 cm and a height of 8 cm, and target T_2 has a diameter of 8 cm and a height of 10 cm.

The first case to be considered is an open-top empty chamber where the dielectric constant for both targets, assumed to be lossless in this case, is set to $\epsilon_r = 3$. Note that an empty air-filled chamber is highly resonant if completely enclosed by the PEC boundaries, therefore to effectively test the imaging performance on the type of data being collected the top boundary is removed, thereby reducing the quality factor of the chamber. For the second case, a partially filled closed-top chamber is considered. In this case, the complex dielectric constant of the targets is set to $\epsilon_r = 4.06 - j0.56$.

To generate synthetic data from the targets 24 transmitter/receiver points were utilized where any of the

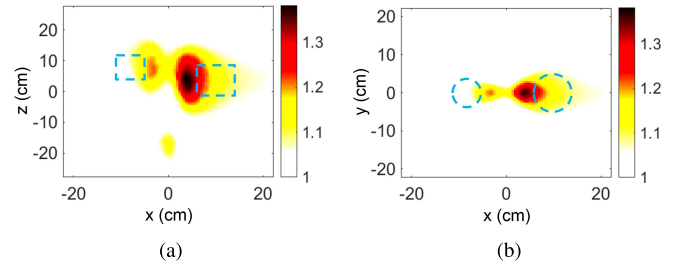


Fig. 3. 2-D cross sections of the real part of the reconstructed permittivity at 722.5 MHz at (a) $y = 0$ and (b) $z = 6$ cm planes when the normal component of the electric field was used for data collection and inversion inside an empty open-top chamber. Dashed lines: true location of the targets.

electromagnetic field components could be collected or a dipole source could be imposed as a transmitter. These transmitter (Tx) and receiver (Rx) points were distributed in four circumferential layers on the walls of the PEC enclosure. In each circumferential layer, six transmitters were positioned 1 cm and 2 cm from the chamber wall for the tangential magnetic sources and the normal electric sources, respectively. The transmitters were ϕ - and z -oriented magnetic dipoles for the magnetic sources and were radially oriented dipoles for the electric sources. Each circumferential layer of Tx-Rx points is rotated by 15° with respect to a neighboring layer (above or below). The receiver locations coincide with the transmitter locations and data were collected for each Tx-Rx pair. Thus, the total amount of collected data are $24 \times 24 = 576$.

A. Inversion Results for Air-Filled Chamber

The interior region of the open-top metallic chamber was discretized using tetrahedral elements. The first step was to collect numerical data using the FEM forward solver. The total number of tetrahedra used in the FEM mesh for the forward solve for this first case was 336723 with the regions R_1 and R_2 both set to air. To avoid an inverse crime, in addition to different FEM meshes being used for the forward and inverse problems, 5% uniformly distributed noise is added to the synthetically generated scattered-field data as per [14]. Addition of noise also helps mimic real measurement systems.

For the inversion mesh, the total number of tetrahedra in the complete mesh was 317685. Note that the imaging domain was restricted to consist of only the spatial region within a cylinder with a radius of 22 cm and a height of 55 cm, centered in the chamber. Reconstruction results for the open-top imaging system when the ρ -component of the electric field is used for the transmitters and receivers are shown in Fig. 3. These results are for a frequency of 722.5 MHz. It can be observed that the targets are successfully reconstructed in a qualitative sense: although the two objects are clearly discernible and the relative sizes are correctly identified, with the right object in Fig. 3 being larger than the left, the actual sizes, locations, and reconstructed permittivity of the targets are not very accurate. The reconstructed permittivity of the targets is lower than its true value, and the percent error in the reconstruction result is 10.43%. It is worth noting that this reconstruction was obtained with limited data (24×24) and that the targets are quite small compared with the wavelength

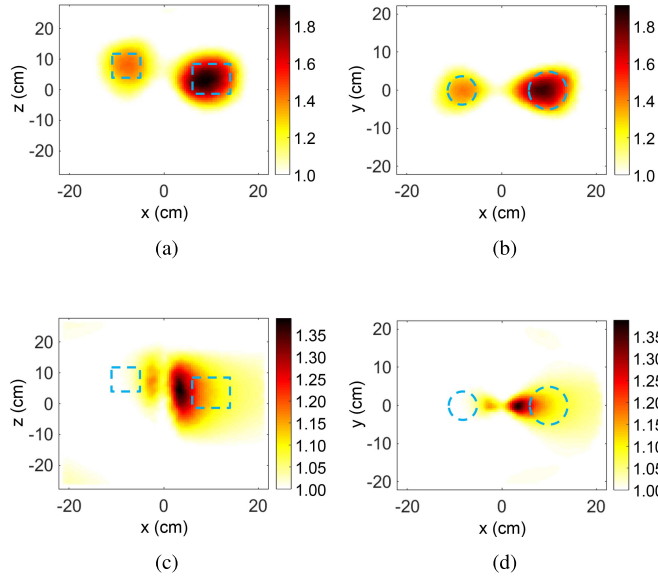


Fig. 4. 2-D cross sections of the real part of the reconstructed permittivity at 722.5 MHz when (a) and (b) ϕ and (c) and (d) z projections of the magnetic field due to magnetic dipoles polarized along ϕ and z axis were collected for inversion inside an empty open-top chamber, respectively. Dashed lines: true location of the targets.

(the largest dimensions of T_1 and T_2 were $\lambda/5$ and $\lambda/4$, respectively).

The reconstructions can be improved by collecting more data via the use of multifrequencies and/or increasing the number of Tx/Rx pairs. We now show that inverting on the tangential components of the surface current produces better results for the same amount of data.

To demonstrate the effect of utilizing the surface currents, the same problem was tested with the tangential, ϕ and z , components of the magnetic field used as data, in conjunction with the tangential magnetic current sources, as opposed to the normal component of the electric field in the previous example (i.e., ρ polarized electric fields and sources). Inversion results are shown for both polarizations in Fig. 4. Although both polarizations provide good qualitative detection of the targets, the ϕ component case provides more accurate reconstruction of the dielectric profiles of the targets, and this imaging performance is robust with respect to frequencies. The percent errors in the reconstruction results when H_z and H_ϕ are used are 10.29% and 8.27%, respectively. Note that the reconstruction result obtained using only the H_z component is similar to that of using only the E_ρ component in that the reconstruction lacks accuracy in localization of the targets as well as their permittivity. One of the important factors for this poor performance is the distribution of the fields within the chamber at the imaging frequency. When Hertzian dipoles normal to the chamber wall are used as sources, and the ρ -projected electric fields are collected, the distribution of the electric field is such that, for most of the transmitters, there exist a null at the center of the chamber (along the height of the chamber) with the targets having minimal effect on the distribution of the electric field. Similar behavior is observed when the z -polarized magnetic dipoles are used as transmitters, and z -polarized magnetic fields are collected. However, when

the ϕ -polarized magnetic sources are used as transmitters and the ϕ -polarization of the magnetic field is collected at the receiver locations, it is noticed that the presence of the targets considerably perturbs the distribution of the magnetic field at the receiver points for most of the transmitters. This significant perturbation of the distribution of the field helps the algorithm better reconstruct the dielectric profile of the targets. Of course, a combination of the different polarizations could be used, but it is difficult to generalize as to what combination would be optimal. In fact, the optimal configuration is most likely target-dependent.

B. Inversion Results for Partially Filled Closed-Top Chamber

For the second case of a partially filled chamber, a total of 345 001 tetrahedra were used in the forward problem with region R_2 set to air and R_1 set to the lossy dielectric constant for the grain. For the inversion, a total of 341 938 elements were used, and the homogeneous grain in the lower part of the chamber was introduced as prior information [16]. That is, the top region, R_2 , was set to air, and the bottom region, R_1 , was set to the dielectric constant of the grain. We call this introducing perfect prior information, and the objective here is to determine whether inhomogeneous targets within the grain can be detected using the normal electric field or the tangential magnetic field components as data.

Note that although perfect prior information is introduced, the complex permittivity variables at the centroid of each tetrahedron inside the imaging domain within the inhomogeneous background are considered free variables in the nonlinear optimization problem. Thus, although a substantial amount of prior information is provided, the inversion algorithm still operates on all the unknowns inside the imaging domain. The only difference is that the contrast is defined with respect to the inhomogeneous background that has been introduced as prior information.

Reconstruction results of the real part of the complex permittivity for the closed-top imaging system when the normal component of the electric field as well as when the tangential components of the magnetic field (H_ϕ and H_z) were used to image the targets at 618 MHz are shown in Fig. 5. Similar results were obtained for the imaginary part of the complex permittivity. It can be observed that the reconstruction results are successful in all the three cases, with some artifacts being visible when the electric field is used. This is due to the fact that because of the small amount of loss inside the inhomogeneous media, the resonance inside the chamber is not strong enough to overshadow the effect of the targets on the field distribution within the chamber, as it was for the empty chamber. It is worth noting that the percent error in the reconstruction results for the cases when E_ρ , H_ϕ , and H_z are used and the true value of the targets are 4.6%, 2.5%, and 3.0%, respectively. Having confirmed the theoretical feasibility of using tangential magnetic field components, directly corresponding to surface currents on the chamber walls, as inversion data, the practical feasibility of obtaining this data with enough accuracy must be verified.

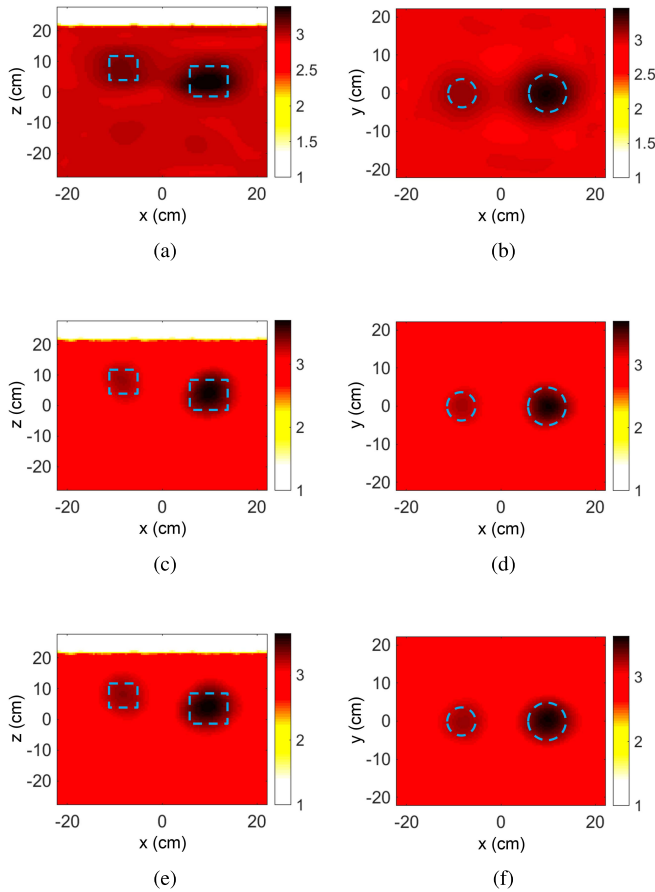


Fig. 5. 2-D cross sections of the real part of the reconstructed permittivity at 618 MHz when (a) and (b) ρ -projection of the electric field due to ρ -polarized Hertzian dipoles, (c) and (d) ϕ , and (e) and (f) z projections of the magnetic field due to magnetic dipoles polarized along ϕ and z -axis were collected, inside a partially filled closed-top chamber, for inversion, respectively. Dashed lines: true location of the targets.

IV. EXPERIMENTAL PROTOTYPE

In this section, we describe the experimental system that was designed and built to validate the concept of using tangential magnetic field components inside resonant imaging chambers, with special emphasis on imaging within the partially filled chambers. For the transmitting and receiving antennas, coaxial, shielded magnetic half-loop antennas were designed, built, and tested. A simple numerical inversion model was adopted for this imaging system where the transmitting antenna was modeled as a magnetic current source.

A. System Configuration

A cylindrical metallic chamber with a height of 86.36 cm and a radius of 28.58 cm, similar to that of the synthetic study, was utilized for the experimental system. Multiple experimental tests incorporating two targets within this chamber, configured either as an air-filled open-top and a closed-top partially field chamber were conducted. In the partially filled tests, the chamber was filled with hard red winter wheat having a moisture content of 9%. It is worth noting that if the chamber is thought of as an open-ended waveguide, the first resonant mode is the TE_{11} mode having a cutoff of 307.6 MHz, whereas

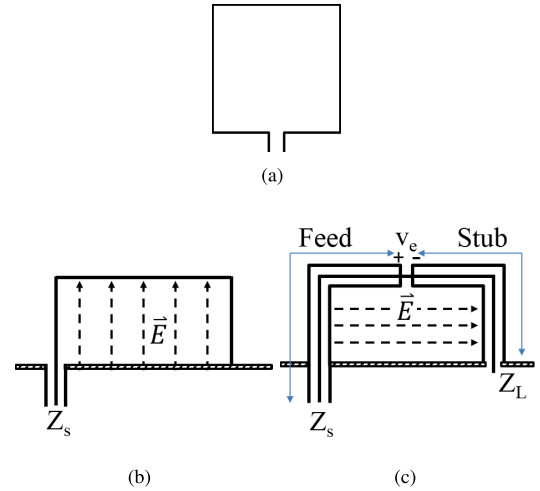


Fig. 6. Magnetic field antennas. (a) Loop antenna. (b) Half-loop antenna. (c) Shielded half-loop antenna.

if it is considered to be a closed circular cavity, the cutoff frequency for the dominant TM_{010} mode is 232.6 MHz.

A block diagram of the experimental imaging system is provided in Fig. 1. This system is comprised of a total of 24 magnetic loop antennas that are equally distributed on the periphery of the chamber wall in four circumferential layers (each having six equally distributed antennas). For the experimental setup, the surface of the loop antennas is placed normal to the axis of the chamber, making each antenna sensitive to the z -polarized magnetic field (or the ϕ component of the surface current). That is, each antenna excites or collects (when used as a transmitter or receiver) the z -polarized, tangential component of the magnetic field close to the chamber wall. The antennas are connected to a 2×24 matrix switch that enables each antenna to either deliver microwave energy to the imaging chamber or collect the magnetic field energy. The matrix switch is connected to a vector network analyzer (VNA), used as the transmitter/receiver. After calibrating the data collected by the VNA (described in Section IV-D), it is used as input to the multiplicatively regularized (MR) FEM-CSI inversion algorithm to reconstruct the electrical properties within the chamber. Fig. 1 shows the location of an example imaging domain \mathcal{D} with respect to the chamber boundaries. The complex dielectric profile of the targets is reconstructed within this domain, which may extend to the walls of the imaging chamber and can be chosen of various shapes.

B. Magnetic Field Antenna

In order to measure the tangential surface currents, the most common antenna type is a simple loop antenna shown in Fig. 6(a). This antenna is easy to design and build and its size can be reduced by half when placed on an electrically conducting plate [Fig. 6(b)]. One of the main disadvantages of this antenna, however, is its sensitivity to the incoming electric field (parallel to the axis of the loop). Close to a PEC surface, the tangential component of the electric field vanishes, and the normal electric field to the PEC becomes dominant. Consequently, close to the chamber wall, in addition to the

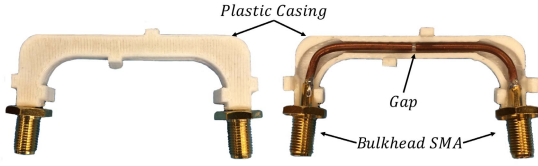


Fig. 7. Coaxial shielded half-loop antenna built for the prototype system.

loop currents due to the magnetic field within the chamber, there will be currents induced, due to the electric field, on the side arms of the loop. It should also be noted that even though the tangential components of the electric field are small, they can still induce a current on the loop antenna. Thus, the measured field at the receiving antenna will be a combination of the electric and magnetic fields [17], [18]. This can have negative effects on the inversion process due to the ambiguity between the calculated fields in the inversion model (which must be specified as a particular type, E or H , and polarization at each receiver location) and the measurements made in the system. To minimize the effects of the electric field on the receiving antennas and to be able to isolate the measured magnetic field from the electric field impinging on the antennas, a coaxial shielded half-loop antenna, as shown in Fig. 6(c), is utilized. This type of loop antenna is simply built by replacing the loop antenna of Fig. 6(b) with a coaxial cable with a gap in its outer conductor. Due to the symmetry of the antenna, the common-mode currents on the outer connector get canceled, and the main contributing current to the measured field at the feed port of the antenna is related to the potential at the gap (from the center conductor to the outer shield). In this antenna, the length of the coax extending out from the feed port to the gap acts as a transmission line. Thus, the effective impedance at the gap is Z_s transformed by the length of the feed line to the gap location. The coaxial section extending from the gap to the load can be thought of as a stub, which can be used to tune the resonant frequency of this antenna [19]. The voltage V_e across the gap can be approximated as [19], [20]

$$V_e = -j\omega\mu HA \quad (6)$$

where A is the geometrical area of the half loop. Analytical equations to model and analyze the performance of these antenna types can be found in the literature [17], [19].

As mentioned earlier, an important deciding factor in the performance of the inversion algorithm, utilizing measurement data, is having an accurate model of the imaging system. This includes the geometry of the imaging system as well as the appropriate models for the utilized sources and collected fields. Ambiguities, or poor approximations, in any of the aforementioned can result in poor reconstructions. The coaxial shielded half-loop antennas are relatively simple to model and were thus chosen for the measurement system. RG405 semi-rigid coaxial cable and SMA bulkhead connectors were used to build the antennas. Cutting the gap at the center of the coaxial cable compromises the mechanical integrity of the antenna. Thus, to protect the antennas from damage, a plastic casing was made using a 3-D printing technology. The fabricated antenna and its support are shown in Fig. 7.

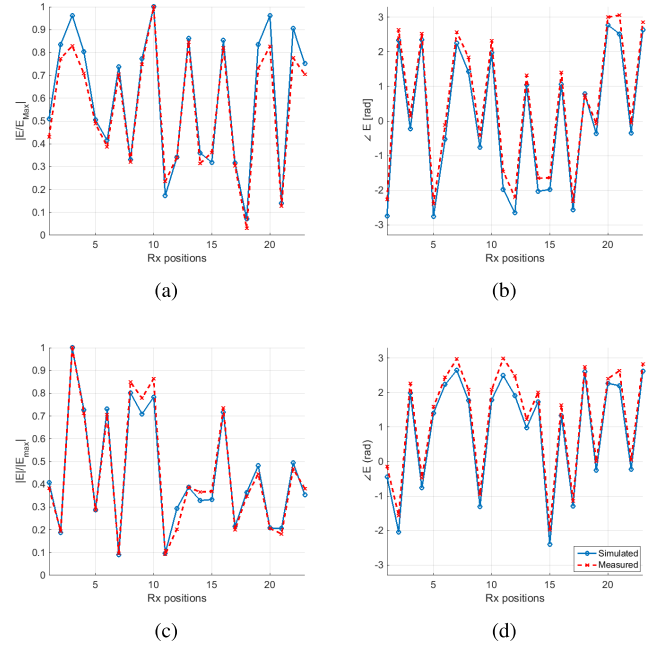


Fig. 8. Plot of the normalized magnitude and phase of the measured S_{21} versus simulated electric field inside the open-top chamber at the receiver locations for (a) and (b) transmitter in the first layer from bottom of the chamber and (c) and (d) transmitter in the second layer from bottom of the chamber. Note that the first Rx position represents the location of the first antenna (excluding the transmitter) on the bottom layer, and the rest of the position numbers correspond to the location of the rest of the antennas moving clockwise per layer starting from the bottom layer.

C. Numerical Model for the System

The numerical model created for the measurement system consists of a cylindrical PEC chamber with antennas excluded in the model. From a received field point of view, the close proximity of the antennas to the chamber wall does not perturb the fields within the chamber significantly and thus they do not need to be modeled. This was also found to be true when short or RAs were used to receive the normal component of the field at the wall [11]. The chamber top was modeled as an absorbing boundary condition for the open-top case and was modeled as a PEC plane for the fully enclosed chamber. The sources were modeled as magnetic dipoles, and the tangential component of the magnetic field was collected at a distance of 1 cm from the chamber wall. This distance locates the transmitters and receiver points at the center of the surface of the loop antenna. To compare the effectiveness of the measurement system to its numerical model, different antennas in the measurement system were used as transmitters while data was collected at the receiver locations. The FEM solver from the inversion code was used to calculate the field values at the same receiver locations due to the magnetic sources. The plots of Fig. 8 show the measured S-parameters using the system shown in Fig. 9 as well as the simulated magnetic fields (normalized magnitude and phase). The normalized measured S_{21} parameter as well as the simulated magnetic field at 23 receiver points are shown for two different transmitters at 0.7225 GHz. These results show that an accurate numerical model of the measurement system is obtained, even with a very simple model.



Fig. 9. Experimental setup (a) with and (b) without grain.

D. Measurement Data Calibration

The measurement data are the S_{21} values between different transmitter and receiver pairs. However, for proper inversion of the measured data, the MR-FEM-CSI algorithm requires calibrated magnetic field values, which better correspond to the inversion model. Different calibration techniques have been reported in the literature [21]–[23], but these need to be appropriately modified so as to apply to the inhomogeneous background case considered herein. For instance, the incident field is defined as the field when the chamber is partially filled with grain. Therefore, to apply the so-called incident-field calibration technique, measurements are required under these circumstances. Thus, in addition to the total field, U^{tot} (where U denotes the S_{21} measurement), measured when the targets are in place, for the air-filled chamber, an incident-field measurement, U^{inc} , of the empty chamber is required, whereas, for the partially filled chamber, an incident-field measurement, $U^{\text{inc|bkgrd}}$, for the partially filled chamber is required (where the properties are assumed to be known).

For an active transmitter t and a receiver r , the calibrated scattered-field using this technique is given as

$$H_{r,t}^{\text{sct, cal}} = \frac{H_{r,t}^{\text{inc}}}{U_{r,t}^{\text{inc}}} (U_{r,t}^{\text{tot}} - U_{r,t}^{\text{inc}}) \quad (7)$$

where $H_{r,t}^{\text{inc}}$ is the simulated incident-field from the numerical model. Note that for the partially filled case, $H_{r,t}^{\text{inc}}$ and $U_{r,t}^{\text{inc}}$ are replaced with $H_{r,t}^{\text{inc|bkgrd}}$ and $U_{r,t}^{\text{inc|bkgrd}}$ in this equation.

The factors $H_{r,t}^{\text{inc}}/U_{r,t}^{\text{inc}}$, for each transmitter/receiver pair, form a vector of calibration coefficients for the inversion model.

E. Inversion of the Measured Data Using H_z Polarized Loops

The performance of the imaging system was initially tested by imaging two targets inside the open-top empty chamber shown in Fig. 9. Two cylindrical targets were hung inside the chamber, offset in the z -direction similar to the synthetic targets shown in Fig. 2. For this case, target T_1 has a diameter of 5.5 cm and a height of 6 cm with an approximate permittivity of $\epsilon_r = 3.8$, and target T_2 has a diameter of 6 cm and a height of 7 cm with an approximate permittivity of $\epsilon_r = 4.5$ (these were the measured values). Inversion results for this test are shown in Fig. 10. The inversion mesh for this case contained 317685 tetrahedral elements with the imaging domain limited to approximately 2/3 of the chamber (and centered in the

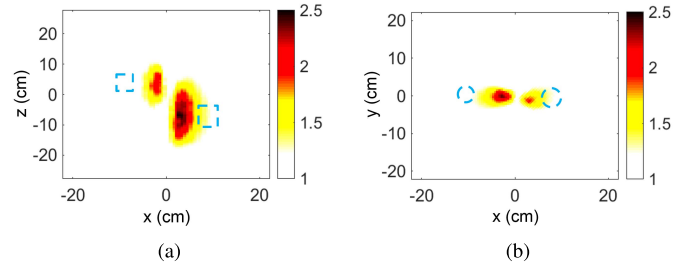


Fig. 10. 2-D cross section of the real part of the reconstructed permittivity for two targets hung inside an open-top empty chamber. (a) $y = 0$ cm plane. (b) $z = 2$ cm plane.



Fig. 11. (a) Spoiled grain and (b) grain-filled measurement chamber. Dashed lines: true location of the targets.

chamber). These results agree with the synthetic analysis conducted in section III-A, where the targets are detected, but poorly localized. Even though the reconstructed permittivities are close to the true values, they are still lower than expected. The poor results are mostly due to the limited amount of information that was used for the inversion: the number of measurements that were made are quite low compared with the number of unknowns (over 211 790). The possibility of using more measurement points as well as more polarizations could improve this result in the empty chamber, but the high Q of the empty chamber is still a factor, which contributes to the poor performance. It contributes in several ways: a poor distribution of the interrogation field within the chamber, poorer calibration of the data (which is not a factor in the synthetic results presented earlier), and the computational accuracy of the numerical model.

The second experimental case that is now considered is when the chamber is filled with grain. Two spoiled grain targets were created by filling plastic containers with wet grain and leaving them for a few days to mold. The targets were submerged in the grain, again offset as in Fig. 2, and data were collected when the imaging chamber was fully enclosed (i.e., with a metallic top). The targets and the imaging chamber are shown in Fig. 11. Target T_1 has a diameter of 6.5 cm and a height of 9.5 cm whereas target T_2 has a diameter of 6 cm and a height of 9 cm. The permittivities of targets T_1 and T_2 were measured to be approximately $\epsilon_r = 4.81 - j0.53$ and $\epsilon_r = 4.2 - j0.43$.

It is worth noting that to ensure that the plastic containers did not affect the imaging results, they were initially filled with uncontaminated grain and placed at the target locations. The field due to the containers was then compared with that of the chamber with no targets (grain only), and no difference was observed.

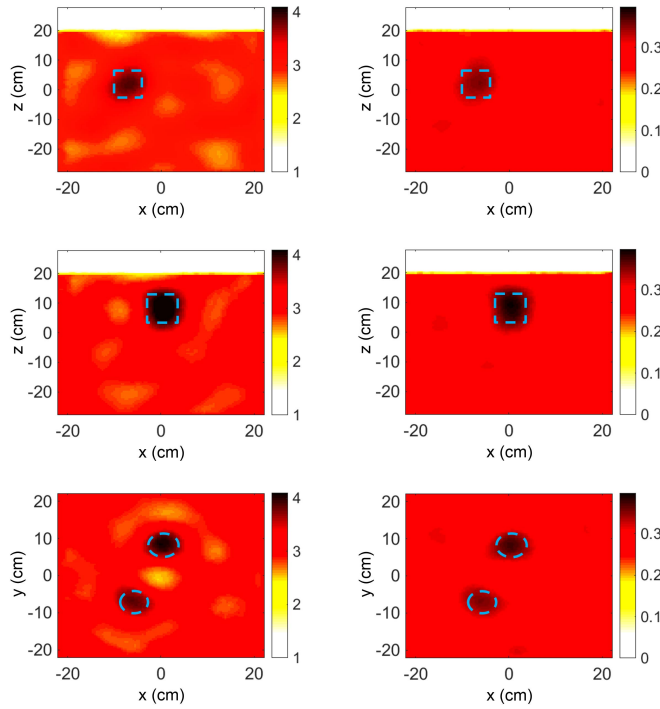


Fig. 12. 2-D slices of the reconstructed complex permittivity at 618 MHz for the two spoilage regions embedded within grain for a partially filled closed-top chamber. Left column: results for the real part of the reconstructed permittivity. Right column: results for the imaginary part of the reconstructed permittivity.

Inversion results for this case are shown in Fig. 12. Note that an approximate level and permittivity for the uncontaminated grain were provided to the inversion algorithm as prior information. The surface of the grain inside the chamber was nonuniform with peaks and valleys having a level that varied by over 7.5 cm (60.36 to 67.86 from the bottom of the chamber). However, it was modeled as a flat surface at a height of 63.36 cm from the bottom of the chamber. This level was also changed, and the inversions showed that as long as the modeled height of the grain was within 60.36–67.86-cm range, the spoilage regions could be reconstructed successfully with minor artifacts when getting closer to the boundaries of this range. The inversion mesh for this case contained 427931 tetrahedral elements.

It can be observed that both targets are successfully reconstructed. The artifacts showing up in these images can be reduced by more accurately modeling the surface of the grain as well as its permittivity (this is the prior information used for the inversion). This was confirmed by the improved reconstruction results (not shown) that were obtained when the grain surface was artificially flattened and its level was accurately represented in the prior information. It is also worth noting that the algorithm tries to reconstruct the nonuniform grain distribution on the surface. This is clearly visible in the reconstruction result at the interface between the air and grain regions. A 3-D plot of the real part of the reconstructed permittivity for this case is shown in Fig. 13 using isosurface plots.

Tests show that using multifrequency data can enhance the accuracy of the results. This is due not only to the additional independent data that is provided at these alternate frequencies

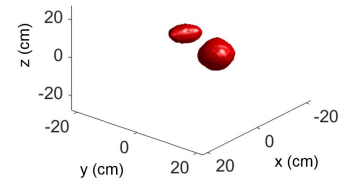


Fig. 13. Isosurface plot of the real part of the reconstructed permittivity.

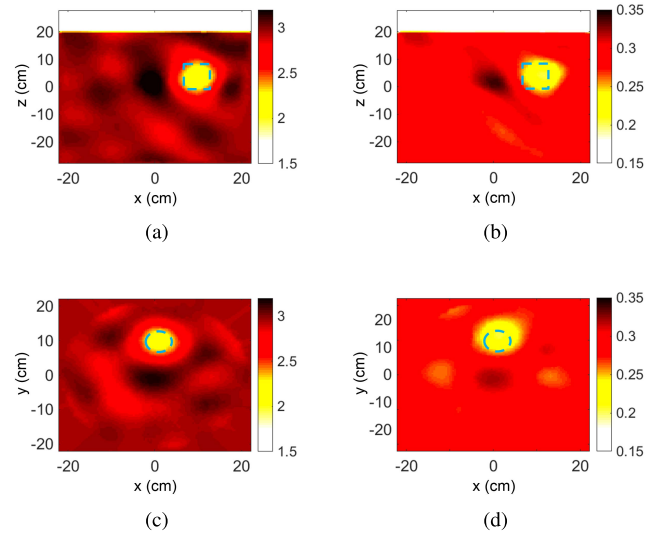


Fig. 14. 2-D cross section of the real (left column) and imaginary (right column) parts of the reconstructed permittivity at 618 MHz for an air void embedded within grain for a partially filled closed-top chamber. (a) and (b) $x = 0$ cm plane. (c) and (d) $z = 6$ cm plane.

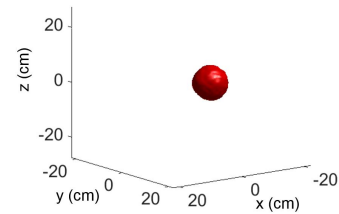


Fig. 15. Isosurface plot of the real part of the reconstructed permittivity.

but also because the resonant modes at each of the frequencies will not be identical. Therefore, some of the low S_{21} data values that are due to the corresponding transmitter–receiver pair occupying positions close to nulls in the modes will only happen at one of the frequencies.

Other than the detection of targets with higher permittivities than the background media, sometimes it is important to be able to detect inhomogeneities that have a lower permittivity compared with the background. (This manifests itself as a negative contrast in the mathematical formulation.) For example, in the grain storage industry, knowing if air voids have formed within the stored commodity is valuable information, because they constitute a danger to humans entering the storage bin. To evaluate the performance of the imaging system for detection of air voids within a grain bin, an empty plastic container was submerged within the grain in the imaging system, and data were collected. Inversion result for this case is shown in Fig. 14. The air void that was introduced into the grain is clearly visible in these images.

A 3-D plot of the real part of the reconstructed permittivity for this case is shown in Fig. 15 using isosurface plots.

V. CONCLUSION

An approach for microwave imaging inside the metallic enclosures is improved and enhanced through the use of surface currents as data for inversion. Coaxial shielded half-loop antennas were successfully utilized to measure the magnetic field, which directly related to the surface currents on the walls of the enclosure. These antennas are low profile and easy to model. Due to small amount of protrusion into the chamber, this type of imaging system can be utilized for monitoring content of storage-units/pipelines, such as grain bins, with minimal modifications needed for the system. Synthetic and experimental results for the grain monitoring application show that using approximate prior information related to the grain level in a partially filled bin provides the inversion algorithm with sufficient information for successful reconstructions.

REFERENCES

- [1] R. Zoughi, *Microwave Non-Destructive Testing and Evaluation Principles*. Norwell, MA, USA: Kluwer, 2000.
- [2] M. Benedetti, M. Donelli, A. Martini, M. Pastorino, A. Rosani, and A. Massa, "An innovative microwave-imaging technique for non-destructive evaluation: Applications to civil structures monitoring and biological bodies inspection," *IEEE Trans. Instrum. Meas.*, vol. 55, no. 6, pp. 1878–1884, Dec. 2006.
- [3] D. M. Sheen, D. L. McMakin, and T. E. Hall, "Three-dimensional millimeter-wave imaging for concealed weapon detection," *IEEE Trans. Microw. Theory Techn.*, vol. 49, no. 9, pp. 1581–1592, Sep. 2001.
- [4] H. G. Wang *et al.*, "Image reconstruction for wet granules by electrical capacitance and microwave tomography," in *Proc. IEEE Int. Conf. Imag. Syst. Techn. (IST)*, Sep. 2015, pp. 1–6.
- [5] A. Abubakar, P. M. van den Berg, and J. J. Mallorqui, "Imaging of biomedical data using a multiplicative regularized contrast source inversion method," *IEEE Trans. Microw. Theory Techn.*, vol. 50, no. 7, pp. 1761–1777, Jul. 2002.
- [6] T. Henriksson, N. Joachimowicz, C. Conessa, and J.-C. Bolomey, "Quantitative microwave imaging for breast cancer detection using a planar 2.45 GHz system," *IEEE Trans. Instrum. Meas.*, vol. 59, no. 10, pp. 2691–2699, Oct. 2010.
- [7] M. Asefi, I. Jeffrey, J. LoVetri, C. Gilmore, P. Card, and J. Paliwal, "Grain bin monitoring via electromagnetic imaging," *Comput. Electron. Agricult.*, vol. 119, pp. 133–141, Nov. 2015.
- [8] P. M. Meaney, M. W. Fanning, D. Li, S. P. Poplack, and K. D. Paulsen, "A clinical prototype for active microwave imaging of the breast," *IEEE Trans. Microw. Theory Techn.*, vol. 48, no. 11, pp. 1841–1853, Nov. 2000.
- [9] D. E. Maier *et al.*, "Monitoring carbon dioxide concentration for early detection of spoilage in stored grain," *Julius-Kühn-Arch.*, vol. 425, p. 505, Sep. 2010.
- [10] M. Asefi, M. Ostadrahimi, A. Zakaria, and J. LoVetri, "A 3-D dual-polarized near-field microwave imaging system," *IEEE Trans. Microw. Theory Techn.*, vol. 62, no. 8, pp. 1790–1797, Aug. 2014.
- [11] M. Asefi, A. Zakaria, and J. LoVetri, "Microwave imaging using normal electric field components inside metallic resonant chambers," *IEEE Trans. Microw. Theory Techn.*, accepted for publication.
- [12] A. Zakaria, M. Asefi, M. Ostadrahimi, I. Jeffrey, and J. LoVetri, "Electromagnetic imaging inside metallic enclosures using the normal boundary field components," in *Proc. USNC-URSI Radio Sci. Meeting, Joint AP-S Symp.*, 2014, p. 253.
- [13] A. Zakaria, I. Jeffrey, and J. LoVetri, "Full-vectorial parallel finite-element contrast source inversion method," *Prog. Electromagn. Res.*, vol. 142, pp. 463–483, Sep. 2013.
- [14] A. Zakaria, C. Gilmore, and J. LoVetri, "Finite-element contrast source inversion method for microwave imaging," *Inverse Prob.*, vol. 26, no. 11, p. 115010, Nov. 2010.
- [15] P. M. van den Berg and A. Abubakar, "Contrast source inversion method: State of art," *Prog. Electromagn. Res.*, vol. 34, pp. 189–218, 2001.
- [16] A. Baran, D. J. Kurrant, A. Zakaria, E. C. Fear, and J. LoVetri, "Breast imaging using microwave tomography with radar-based tissue-regions estimation," *Prog. Electromagn. Res.*, vol. 149, pp. 161–171, Oct. 2014.
- [17] R. J. Spiegel, C. A. Booth, and E. L. Bronaugh, "A radiation measuring system with potential automotive under-hood application," *IEEE Trans. Electromagn. Compat.*, vol. EMC-25, no. 2, pp. 61–69, May 1983.
- [18] J. Dyson, "Measurement of near fields of antennas and scatterers," *IEEE Trans. Antennas Propag.*, vol. AP-21, no. 4, pp. 446–460, Jul. 1973.
- [19] G. S. Smith, "Loop antennas," in *Antenna Engineering Handbook*. New York, NY, USA: McGraw-Hill, 1984, pp. 5–13.
- [20] M. Kanda, "Standard probes for electromagnetic field measurements," *IEEE Trans. Antennas Propag.*, vol. 41, no. 10, pp. 1349–1364, Oct. 1993.
- [21] M. Ostadrahimi *et al.*, "Analysis of incident field modeling and incident/scattered field calibration techniques in microwave tomography," *IEEE Antennas Wireless Propag. Lett.*, vol. 10, pp. 900–903, Sep. 2011.
- [22] M. Asefi, M. Ostadrahimi, J. LoVetri, and L. Shafai, "Analysis of a 3D microwave imaging system," in *Proc. IEEE Antennas Propag. Soc. Int. Symp. (AP-S)*, Jul. 2013, pp. 608–609.
- [23] C. Gilmore *et al.*, "A wideband microwave tomography system with a novel frequency selection procedure," *IEEE Trans. Biomed. Eng.*, vol. 57, no. 4, pp. 894–904, Apr. 2010.



Mohammad Asefi (S'08) received the B.Sc. and M.Sc. (*cum laude*) degrees in antennas and microwave engineering from the American University of Sharjah, Sharjah, United Arab Emirates, in 2009 and 2011, respectively, and the Ph.D. degree in electrical and computer engineering from the University of Manitoba, Winnipeg, MB, Canada, in 2016.

He is currently a Post-Doctoral Fellow with the Electromagnetic Imaging Laboratory, Department of Electrical and Computer Engineering, University of Manitoba. He is also a Co-Founder and the Managing Director of the technology start-up Genuwave Imaging Technologies Inc., Winnipeg, focused on developing microwave imaging systems for biomedical applications. His current research interests include biomedical imaging, breast cancer detection, grain bin imaging, designing and developing microwave imaging systems, near-field measurement, and the modulated scattering technique.



Gabriel Faucher received the B.Sc. degree in applied mathematics, the B.Sc. degree in computer engineering, and the M.Sc. degree in electrical engineering from the University of Manitoba, Winnipeg, MB, Canada, in 2006, 2009, and 2013, respectively.

He is currently the lead Software Developer with the Electromagnetic Imaging Laboratory, University of Manitoba.

Joe LoVetri (S'84–M'84–SM'09), photograph and biography not available at the time of publication.